Materials and Structures (2026) 59:117
https://doi.org/10.1617/s11527-026-03016-5

ORIGINAL ARTICLE

Unlocking concrete's three-dimensional pore structure: a comprehensive micro-CT analysis

Lívia Vásárhelyi · Dániel Sebők · Imre Szenti · Orsolya Szép · Zoltán Kónya · Ákos Kukovecz

Received: 11 March 2025 / Revised: 30 January 2026 / Accepted: 15 February 2026 / Published online: 25 February 2026

Abstract Micro-computed tomography (micro-CT) is widely applied to characterize concrete pore systems; however, analyses are typically limited to global porosity and pore size metrics, providing little insight into the spatial heterogeneity of pores. In particular, three-dimensional, scale-dependent quantification of pore heterogeneity remains largely unexplored. In this study, micro-CT was used to analyze the three-dimensional pore structure of concrete cubes produced with and without the addition of superplasticizer. Beyond conventional porosity descriptors, pore-system heterogeneity was quantified using three-dimensional lacunarity analysis. Pore evolution during curing was investigated, and intact specimens were compared with fractured samples. The results demonstrate that the addition of superplasticizer significantly reduces porosity and average pore size while promoting a more homogeneous pore distribution. Lacunarity reveals a pronounced increase in pore-system heterogeneity during early curing, followed by stabilization, reflecting hydration-driven pore refinement and the increasing dominance of larger detectable pores. Furthermore, fractured regions are shown to be associated with higher contributions from large, spatially heterogeneous pores. The main contribution of this work is the introduction of lacunarity as a robust, scale-sensitive descriptor for concrete pore systems, providing information beyond conventional porosity measures and enabling a more comprehensive understanding of pore structure evolution and fracture-related heterogeneity.

Keywords Microcomputed tomography · Porosity · Spatial distribution of pores · Lacunarity · Concrete · Superplasticizer

1 Introduction

Porosity is a crucial feature in structural materials that affects their quality and performance. The mechanical and insulating properties, as well as the gas or liquid permeability of materials, are all influenced by porosity [1–4]. Generally, an increase in porosity results in a decrease in strength [2]. The significance of air-filled pores, however, varies depending on the material. In bricks, for example, pores play a vital role in thermal insulation, but an increase in porosity can diminish the quality and durability of bricks [5–7]. On the other hand, even the tiniest pore

L. Vásárhelyi · D. Sebők · I. Szenti (✉) · O. Szép · Z. Kónya · Á. Kukovecz (✉)
Interdisciplinary Excellence Centre, Department of Applied and Environmental Chemistry, University of Szeged, Rerrich Béla tér 1, 6720 Szeged, Hungary
e-mail: szenti.imre@szte.hu

Á. Kukovecz
e-mail: kakos@chem.u-szeged.hu

I. Szenti · Z. Kónya
HUN-REN Reaction Kinetics and Surface Chemistry Research Group, Rerrich Béla tér 1, 6720 Szeged, Hungary

can have adverse effects on the structural integrity of metal parts [8]. In the case of concrete, minimizing the pore content aims to produce harder and more durable concrete [9]. Conversely, foamed concrete has intentionally higher porosity to reduce weight and improve thermal properties, at the expense of strength [10].

Various techniques have been developed to measure the porosity of a wide range of materials, such as mercury intrusion porosimetry [11] or helium pycnometry [12]. These conventional techniques enable the determination of porosity on a wide scale, ranging from nanopores to macropores, but they only account for the open porosity of materials. Imaging techniques, such as scanning electron microscopy [13] or confocal laser scanning microscopy [14], are capable of determining closed pores, but at the expense of sample destruction. These imaging techniques also require extensive sample preparation, a considerable amount of time, and significant effort. High-resolution computed tomography (micro-CT) is a powerful non-destructive imaging tool capable of investigating the total porosity in three dimensions without causing harm to the sample. With virtually no sample preparation required, it is able to investigate relatively large volumes. Despite its inferior spatial resolution, technical advancements have enabled micro-CT to achieve submicron resolution [15]. As a dynamically spreading three-dimensional X-ray imaging tool in materials science [16, 17], micro-CT provides detailed quantitative data about numerous aspects of the porosity of materials and gives a real 3D visualization of the pore structure. The high Z contrast between the components of the sample is one of the most important criteria for obtaining high-quality imaging. Micro-CT is especially suitable for investigating porous materials [18, 19], as the air and the sample matrix have highly different X-ray absorption properties. It enables the investigation of individual pores and provides insight into not just the porosity, but also the pore size distribution, size, and shape of individual pores and their spatial distribution. Its non-destructive nature allows for investigating the samples in situ, following the changes caused by external forces, such as mechanical forces like uniaxial compression or tension, and determining the changes in the pore structure. However, the image processing and segmentation of micro-CT imaging can introduce a serious human error factor into the process [20–22]. Several segmentation algorithms and thresholding techniques have been developed to identify the different phases inside the samples [23–26], with the Otsu algorithm being the most commonly used [27]. Another recently popular approach is the use of artificial intelligence in the segmentation process [28, 29].

The scientific literature on porosity analysis tends to focus on a single number showing the proportion of solid and void in a material, while neglecting other important factors such as the size, shape, and spatial distribution of pores [2, 30]. Inhomogeneous pore distribution can lead to structural problems, with pore-rich parts being the starting point of breaks, cracks, and mechanical deformations. Imaging techniques have the advantage of being able to investigate the spatial distribution of pores, which can be quantitatively described by lacunarity (Λ). Lacunarity is a measure of the spatial heterogeneity of samples [31] and is capable of describing the deviation from translational homogeneity [32] in one, two, or three dimensions. It is one of the most valuable descriptors of spatial heterogeneity of pores in materials and can have a direct effect on physical properties [33, 34]. Still, it is a lesser-known feature in the micro-CT community, since calculating lacunarity for real-life large 3D micro-CT datasets using the most widespread gliding-box method (GBM) is very time-consuming [35, 36]. Using a simplified approach called the fixed-grid method (FGM) [37] for the calculations can result in fast and accurate lacunarity curves, making lacunarity calculations available and feasible for a much wider audience.

To calculate lacunarity, the $M \times M \times M$-sized volume of interest (VOI) is divided into $\varepsilon \times \varepsilon \times \varepsilon$-sized boxes, and their masses (P) are calculated (for binary images, the mass means the number of white voxels). $Q(P, \varepsilon)$ probability distribution is calculated by dividing the number of ε-sized boxes containing P white voxels ($n(P, \varepsilon)$) by the number of possible box positions ($N(M, \varepsilon)$) (Eq. 1).

$$Q(P, \varepsilon) = \frac{n(P, \varepsilon)}{N(M, \varepsilon)} \tag{1}$$

The first (Eq. 2) and second (Eq. 3) moments of the distribution are calculated, and they are used to determine the lacunarity at a given box size (Eq. 4).

$$Z^{(1)} = \sum_{\varepsilon} PQ(P, \varepsilon) \tag{2}$$

$$Z^{(2)} = \sum_{\varepsilon} P^2 Q(P, \varepsilon) \tag{3}$$

$$\Lambda(\varepsilon) = \frac{Z^{(2)}}{\left(Z^{(1)}\right)^2} \tag{4}$$

The main difference between the gliding box method (GBM) and the fixed grid method (FGM) lies in the sampling strategy applied during the lacunarity calculation. While GBM employs overlapping boxes, FGM considers only non-overlapping boxes, which significantly reduces computational demand and calculation time [37]. Lacunarity is typically evaluated as a function of box size, and the shape of the resulting lacunarity curve provides insight into the spatial organization of a structure. From this scale-dependent behavior, conclusions can be drawn regarding structural heterogeneity, and hidden patterns or regularities may be identified even in systems that appear highly disordered [38, 39].

From a physical perspective, lacunarity quantifies the spatial heterogeneity of a pore system by describing how voids are distributed within a material. High lacunarity values indicate pronounced heterogeneity, characterized by pore clustering and the presence of large pore-free regions, whereas low lacunarity values correspond to a more homogeneous and evenly distributed pore structure. Unlike conventional porosity measures, lacunarity is sensitive to the spatial arrangement of pores; consequently, materials with similar porosity and pore size distributions may exhibit fundamentally different heterogeneity levels. The scale dependence of lacunarity further enables the identification of characteristic length scales and clarifies the relative contribution of small and large pores to the overall heterogeneity of the material. Owing to these properties, lacunarity has been successfully applied to characterize pore-system heterogeneity in a wide range of materials, including geological samples [40–42] and biomaterials [43, 44].

Concrete is a crucial building material, and an in-depth understanding of its inner structure is indispensable for effectively working with it and changing its properties according to specific purposes. While micro-CT is routinely used in concrete research [45–48], a detailed characterization of the pore structure is still lacking. The pore structure of concrete is a crucial property of its strength [49]. Uneven pore distribution in concrete can lead to a decrease in strength and create weak spots [5, 6, 30], endangering the structural integrity of buildings. Porosity and pore clustering affect the insulating properties [50] and permeability of concrete, with porosity, shape, size, connectivity, and tortuosity of pores all playing a part [51]. The pore distribution can also affect thermal and mechanical characteristics [52].

The spatial heterogeneity of concrete, particularly in the context of pore size distribution, has been a subject of interest in recent research. Jain et al. developed a model that considers the heterogeneous nature of the concrete microstructure in changing environmental conditions [53]. Similarly, Castillo et al. modelled the mechanical behavior of concrete with spatially varying material properties [54]. Le et al. explored the effect of heterogeneity on the chloride penetration of reinforced concrete [55]. Gao et al. proposed a method based on meso-scale modeling for locating damage in heterogeneous concrete material [56]. Carpinteri et al. discussed the modeling of damage in concrete using stochastic lacunar fractal sets, emphasizing the spatial characteristics of concrete [57]. In a broader context, Chongkai et al. [58] and Chhun et al. [59] addressed the stochastic process of corrosion of steel bars and the probabilistic scale effect caused by material heterogeneity, respectively. Gabriel-Wettey et al. investigated how the porosity and compressive strength of concrete vary as a function of the concrete's curing time [60].

Given that concrete is an extensively investigated material with micro-CT, and its pore structure has a significant effect on various properties, in this work it was chosen as a model system for detailed porosity analysis, with special emphasis on the spatial distribution of pores. Additives, such as superplasticizers, can affect the pore structure of concrete [61, 62], i.e., decrease porosity and pore size and create a more even pore size distribution. Thus, two different concrete types were compared in several different aspects of porosity: one made with the traditional recipe and one with superplasticizer additives. To this end, ten cubic concrete samples were created as model samples, with five made by the traditional recipe and the other five with superplasticizer added, for the investigation of different pore structures, such

as porosity, number, and size of pores, among others. The porosity of concrete and the spatial distribution of its pores are significantly influenced by the curing process. Therefore, this study examines the evolution of porosity and pore distribution in additive-free concrete as a function of curing time. All the samples were scanned with a high-resolution micro-CT for detailed characterization and comparison of their pore structure. The spatial heterogeneity of pores was also investigated and described by lacunarity calculations using our self-developed software [37]. Uniaxial compressive tests were conducted to examine the differences between the broken and residual parts of the samples in terms of porosity and lacunarity of pores. To the best of our knowledge, lacunarity of the 3D pore structure of concrete samples has not been investigated before. Furthermore, the investigation of broken and residual parts of cubic concrete samples and the comparison of these parts in terms of porosity is a novel concept as well.

2 Materials and methods

2.1 Sample preparation

Fifteen $3 \times 3 \times 3$ cm^3 concrete cubes were prepared for the investigation. For the traditional concrete samples (TC), Portland Composite Cement (EN 197-1 CEM II/B-M (V-LL) 32,5 N, DDC Beremend) was used as a binder, mixed with $d > 1$ mm sand. For the other type of samples (SPC), superplasticizer (VIP-Rex SF, Vip-Rex Kft., Kisújszállás) was added to the mixture. Ten TC and five SPC samples were prepared (their exact composition is shown in Table 1), five–five TC and SPC samples were cured for 28 days under water and then dried in ambient conditions until their weight stabilized before micro-CT measurements. Another 5 /five TC samples were used to test the effect of the curing. During the experiment, the concrete cubes were examined by micro-CT after 3, 7, and 28 days.

Table 1 Composition of the different types of concrete samples

Sample	Sand (g)	Cement (g)	Water (mL)	WtC *	SP ** (mL)
TC	446	288	144	0.5	–
SPC	446	288	72	0.25	10

*WtC = water to cement ratio

**SP = superplasticizer additive (~3.5 m/m % for cement)

2.2 Methods

The present study investigated the internal structure of as-prepared concrete cubes using a Bruker Skyscan 2211 Nanotomograph (Skyscan, Bruker, Belgium) to obtain micro-CT images and perform a detailed analysis of the pore structure of all ten samples. The micro-CT images were obtained in high-power mode using a 6 Mp flat-panel detector, with a 130 kV tube voltage and 155 µA tube current, and a 50 ms exposure time. A 0.5 mm Cu filter was used, and 1041 projections were taken with a 0.2° rotation step. Each projection is an average of 5 images, and the pixel resolution was 30 µm, resulting in an average scan time of 23 min. For the image reconstruction, NRecon software (Skyscan, Bruker, Belgium) was used, which applies the Feldkamp algorithm [63]; the size of the reconstructed images was 4032×2688 pixels. The most common imaging artifacts (beam hardening, ring artifact, misalignment) were corrected, and defective pixels were masked during reconstruction.

CT-An software (Skyscan, Bruker, Belgium) was used for the detailed analysis of the pore structure of samples. The topmost 20 slices were not taken into account due to their unreliable nature caused by casting error, similar to the bottom slices caused by imaging artifacts because of the X-ray scattering caused by the proximity of the metal sample holder. Segmented images were created using the Otsu algorithm [27], which is a widely accepted, histogram-based global thresholding method, commonly applied in micro-CT analysis of porous materials due to its objectivity and reproducibility. The method determines an optimal threshold by minimizing the intra-class variance between solid and void phases, which is particularly suitable for systems exhibiting high X-ray attenuation contrast, such as concrete and air-filled pores. Unreliable data points that could not be distinguished from noise were removed prior to the 3D porosity analysis; consequently, only pores larger than 90 µm in diameter were considered. This lower detection limit arises from the voxel size of the micro-CT scans (30 µm), which represents the main resolution-related constraint affecting the accuracy of the analysis. Accordingly, the reported closed porosity values correspond to

resolvable closed pores only, while smaller closed pores may remain undetected. Importantly, this limitation does not affect the comparative analysis, as all samples were evaluated using identical imaging, reconstruction, and segmentation parameters. CT Vox (Skyscan, Bruker, Belgium) was used for the visualization of the pores and the sample matrix.

Lacunarity calculations for the pore structures were conducted by our self-developed software Lac3D [37], which uses the fix-grid method to calculate 3D lacunarity within seconds. For the lacunarity calculation, the largest volume of interest (VOI) has a side length (M) of 800 voxels, while for the smaller VOI, $M = 400$.

For localized statistical analysis, the volume-weighted pore-size distribution was divided into three pore-size ranges: small pores (0.06–0.42 mm), medium pores (0.42–0.84 mm), and large pores (> 0.84 mm). This classification was guided by physical considerations and the spatial resolution of the micro-CT measurements. The selected ranges separate resolution-limited fine pores, bulk pores, and volume-dominant large pores, which are known to play distinct roles in pore-network heterogeneity. For each specimen, pore-volume fractions within the defined pore-size ranges were summed, yielding one value per specimen and pore-size class. Differences between TC and SPC groups ($n = 5$ each) were evaluated using two-sided Mann–Whitney U tests, which do not assume normality and are appropriate for small sample sizes.

Finally, a Zwick Roell Zmart Pro instrument was used to compress and break the concrete cubes. A 50 N pre-load was used with a 100 mm/min pre-load speed, while the test speed was 0.5 MPa/s. The cubes were wrapped in Parafilm® M sealing foil to prevent the samples from falling apart, allowing subsequent micro-CT measurements. The rotation and image registration of the images taken at different stages of the samples (before and after compressive tests) were conducted using DataViewer software (Skyscan, Bruker, Belgium).

3 Results and discussion

3.1 Detailed characterization of the pore structures

Micro-CT analysis was conducted on 5–5 samples of each type to provide a detailed characterization of their pore structure. Figure 1 displays the 3D pore structure of representative examples for both TC (Fig. 1A) and SPC (Fig. 1B) samples. The volume-rendered 3D micro-CT images and the pore size distribution diagram (Fig. 1C) reveal a prominent difference between the two sample types. Notably, TC exhibits numerous large pores, while SPC has a narrower pore size distribution.

Micro-CT imaging provides abundant quantitative data in addition to visual information, thereby enabling a precise comparison between two model systems. This is evident from Table 2, which shows that the original 1.46% average total porosity is reduced to 1.20% for the SPC model, resulting in a nearly 20% decrease. Furthermore, the number and size of pores also exhibit a significant change, with the average number of pores increasing from 4191 to 7294, and the size distribution diagram narrowing down for SPC.

The decrease in total porosity, accompanied by an increase in the number of pores, is consistent with a reduction in the average pore diameter, which decreases from 0.51 mm (corresponding to a pore volume of 0.07 mm^3 assuming spherical geometry) to 0.40 mm ($V = 0.033$ mm^3). This trend is further reflected in the pore size distribution, which shifts toward smaller pore sizes, as shown in Fig. 1C. Statistical analysis supports this observation, revealing significant differences between TC and SPC samples in the small-pore (0.06–0.36 mm, $p = 0.0079$) and large-pore (> 0.84 mm, $p = 0.0159$) ranges, while no statistically significant difference was detected in the medium-pore range (0.42–0.84 mm, $p = 1.00$), indicating comparable pore-volume contributions in this size regime.

These findings are consistent with prior literature [61, 64]. Interestingly, the largest individual pore found in any TC sample was 22.9 mm^3, while for SPC, it was only 4.9 mm^3. On average, the largest pore size for TC was 10.85 mm^3, while for SPC, it was only 3.98 mm^3. Furthermore, the presence of extremely large pores (greater than 1 mm in diameter, which is equivalent to 0.52 mm^3 volume for spherical pores) is much more frequent in TC, with an average of 87 in each sample, while only 28 are present in SPC. This implies that 2.08% of all pores are deemed large in TC, whereas only 0.41% of pores are classified as large in SPC.

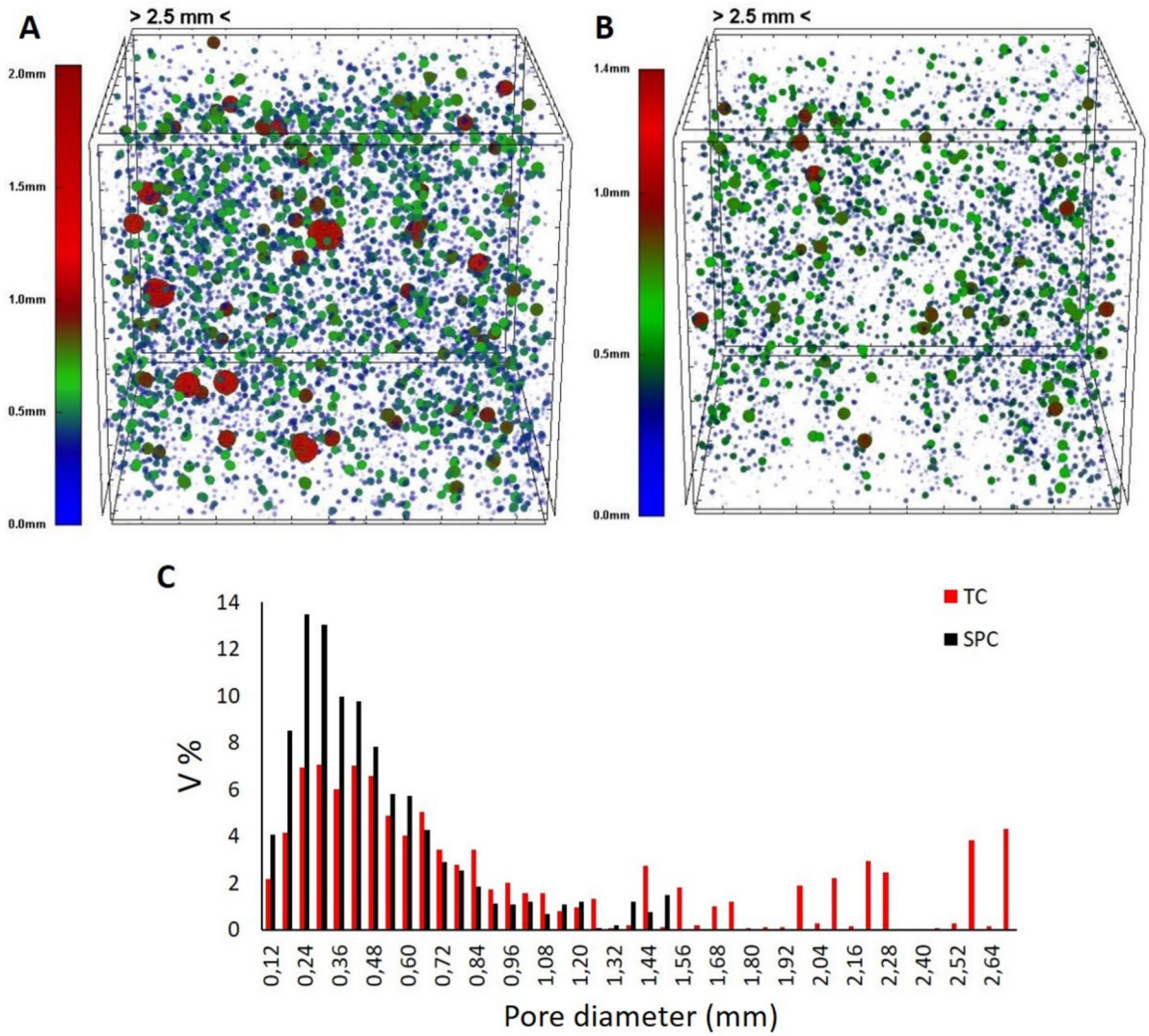

Fig. 1 Pore size distribution of representative examples of **A** TC and **B** SPC. The color bar indicates the average diameter of pores. **C** shows the pore size distribution diagrams for both samples

Table 2 Porosity analysis of the two model systems

	TC	SPC
Total porosity (%)	1.46 ± 0.11	1.20 ± 0.10
Number of closed pores	4191 ± 232	7294 ± 511
Volume of closed pores (mm^3)	294.2 ± 21.8	241.7 ± 19.8
Number of pores/mm^3	0.19 ± 0.01	0.32 ± 0.02
Average pore volume (mm^3)	0.070 ± 0.004	0.033 ± 0.002
Average pore diameter (mm)	0.51 ± 0.03	0.40 ± 0.02

The analysis of the spatial distribution of pores is a vital aspect of porous material characterization, with lacunarity being a crucial parameter in this regard. As depicted in Fig. 2, both types of samples exhibit significant heterogeneity in pore distribution, with curves showing a relatively low steepness (Fig. 2A). However, differences between the two samples are notable, with the pores in SPC exhibiting a more homogeneous distribution than those in TC. The shape of the lacunarity curve is indicative of the structural heterogeneity of the material, and the steeper decline in the lacunarity curve of SPC

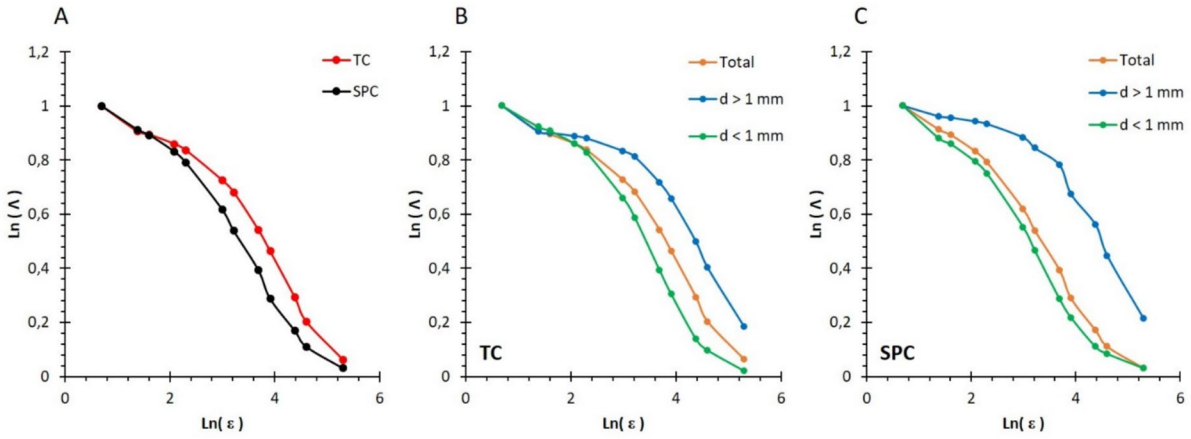

Fig. 2 Representative lacunarity curves **A** of TC and SPC, and the differences in the spatial heterogeneity of small ($d < 1$ mm) and large ($d > 1$ mm) pores for **B** TC and **C** SPC samples

compared to that of TC denotes a higher level of homogeneity in the former sample. Additionally, the lacunarity of extremely large pores (Fig. 2B) differs from that of smaller pores (Fig. 2C), with larger pores being more heterogeneously distributed. For SPC, the lacunarity curve of large pores is more heterogeneous than that of small and total pores, indicating the dominance of a large number of small pores in the total lacunarity, with the effect of the few large pores being less significant. On the other hand, for TC, large and small pores contribute equally to the total lacunarity of the sample. Overall, the analysis of lacunarity is an essential tool in the study of porous materials, providing valuable insights into their structural characteristics and heterogeneity.

The differences between various regions of the samples under consideration were also examined. Specifically, the discrepancies between the entire samples ($M = 800$) and smaller cubic volumes ($M = 400$) located in the center of the cubes were investigated. These volumes were approximately one-eighth of the whole sample. The analysis revealed interesting differences, not only in the spatial distribution of pores but also in the pore sizes.

For instance, for TC samples, the average pore diameter decreased from 0.51 to 0.47 mm within the inner volume. In addition, only 1.7% of all detected pores in the inner region belonged to the large-pore category, compared to 2.08% for the entire specimen. This difference indicates that larger pores are preferentially located near the surfaces of the cubic samples. The preferential occurrence of larger pores in the exterior regions is primarily attributed to casting-related boundary effects, rather than curing-induced drying. During placement, geometric confinement and altered flow conditions in the vicinity of the mold walls promote localized air entrapment and the formation of coarser voids in surface-adjacent regions. These initial structural differences are largely preserved during subsequent water curing. Furthermore, even under water-curing conditions, spatial differences in hydration kinetics may develop: the exterior regions experience direct and continuous water availability, which can accelerate early hydration and locally enhance microstructural heterogeneity, whereas the interior volume undergoes more diffusion-controlled and comparatively homogeneous hydration. As a consequence, larger pores are more frequently observed near the sample surfaces, while the inner regions exhibit a finer pore structure.

Similarly, for SPC, only 0.32% of the pores were large, compared to 0.4% for the whole sample, while the average pore diameter slightly decreased from 0.4 to 0.39 mm. This provides further evidence that smaller pores tend to be more homogeneously distributed than larger pores. It was also found that the largest pore was never located inside the smaller volume at the center for any of the samples, and the average largest pore size decreased to 3.13 mm^3 (from 10.85 mm^3) in the case of TC and to 1.03 mm^3 (from 3.98 mm^3) in the case of SPC. Additionally, the spatial heterogeneity of pores changed for each sample: the

inner volumes ($M = 400$) appeared much more homogeneous (Fig. 3A, yellow for TC and blue for SPC) than the entirety of the samples ($M = 800$) (Fig. 3A, orange for TC and gray for SPC). Furthermore, even the inner volume of TC (Fig. 3A, yellow) was observed to be more heterogeneous than the total volume of SPC (Fig. 3, gray). Finally, in line with the above observations, the lacunarity of large and small pores was different inside the small inner volume. However, the total lacunarity is closer to (Fig. 3B) or almost identical (Fig. 3C) to the lacunarity of small pores. This could be attributed to the smaller number of large pores in the inner volume. Overall, these findings highlight the importance of considering different regions of samples when investigating their properties.

3.2 Effect of curing on the pore structure

Besides additives, the curing time of the cement also affects the porosity of samples and their pore structure. Figure 4 shows the changes observed in the closed pores of the same concrete cube with increasing curing time. The 3D rendered images (Fig. 4A–C) clearly show that the amount of closed pores decreases over time. Considering that Fig. 4C shows the pores that disappear, it can be concluded that during curing, mainly small pores disappear, as confirmed by the size distribution of the pores (Fig. 4D).

After 3 days, 52 V% of the closed pores were smaller than 0.2 mm, whereas after 28 days this proportion decreased to 43 V%, indicating a progressive reduction in the contribution of small closed pores during curing. In parallel, the spatial heterogeneity of the pore system evolved over time, as reflected by the lacunarity values (Fig. 4D, inset): the pore structure became more heterogeneous up to 7 days, after which lacunarity remained nearly constant. The increase in lacunarity during the early curing period is primarily attributed to hydration-induced pore shrinkage combined with resolution-related effects of the micro-CT analysis. As hydration progresses, small pores tend to shrink, and a substantial fraction falls below the spatial resolution limit, reducing their contribution to a spatially uniform pore network. Consequently, the detectable pore system becomes increasingly dominated by larger, less uniformly distributed pores, leading to an apparent increase in heterogeneity during the first 7 days of curing.

The quantitative data calculated from the micro-CT measurements are shown in Table 3. The porosity of the concrete cube decreased by approximately 43%, the number of closed pores by about 51%, while the total volume of the pores decreased by around 40%. These data support the observations made so far.

During concrete curing, the smallest pores tend to disappear, while the size of the remaining pores decreases. This process can be clearly seen in this case, as the total pore volume decreased from 186 to 111.9 mm^3 while the volume of the missing pores

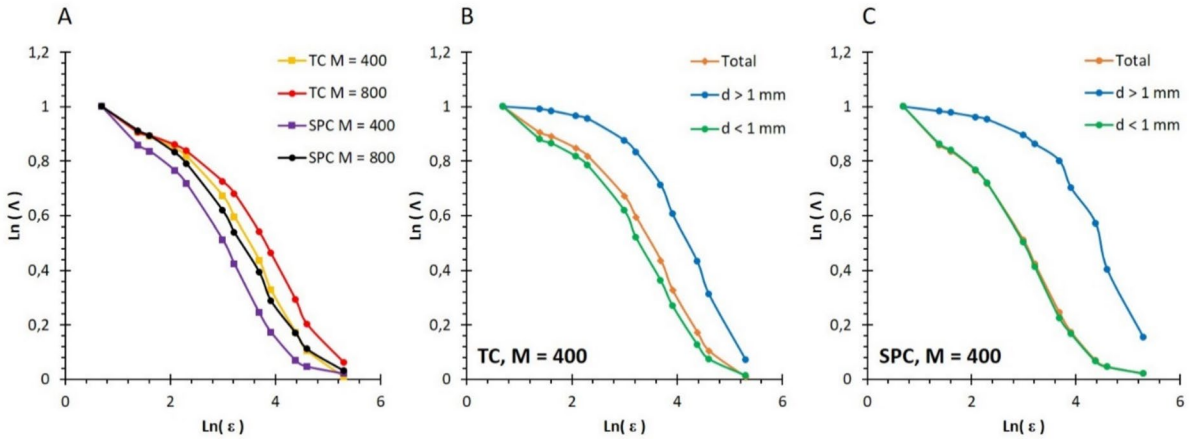

Fig. 3 Lacunarity of **A** the inner ($M = 400$ voxel) and outer ($M = 800$ voxel) parts of samples and the small ($d < 1$ mm), large ($d > 1$ mm), and total pores for the inner volumes of the **B** TC and **C** SPC samples

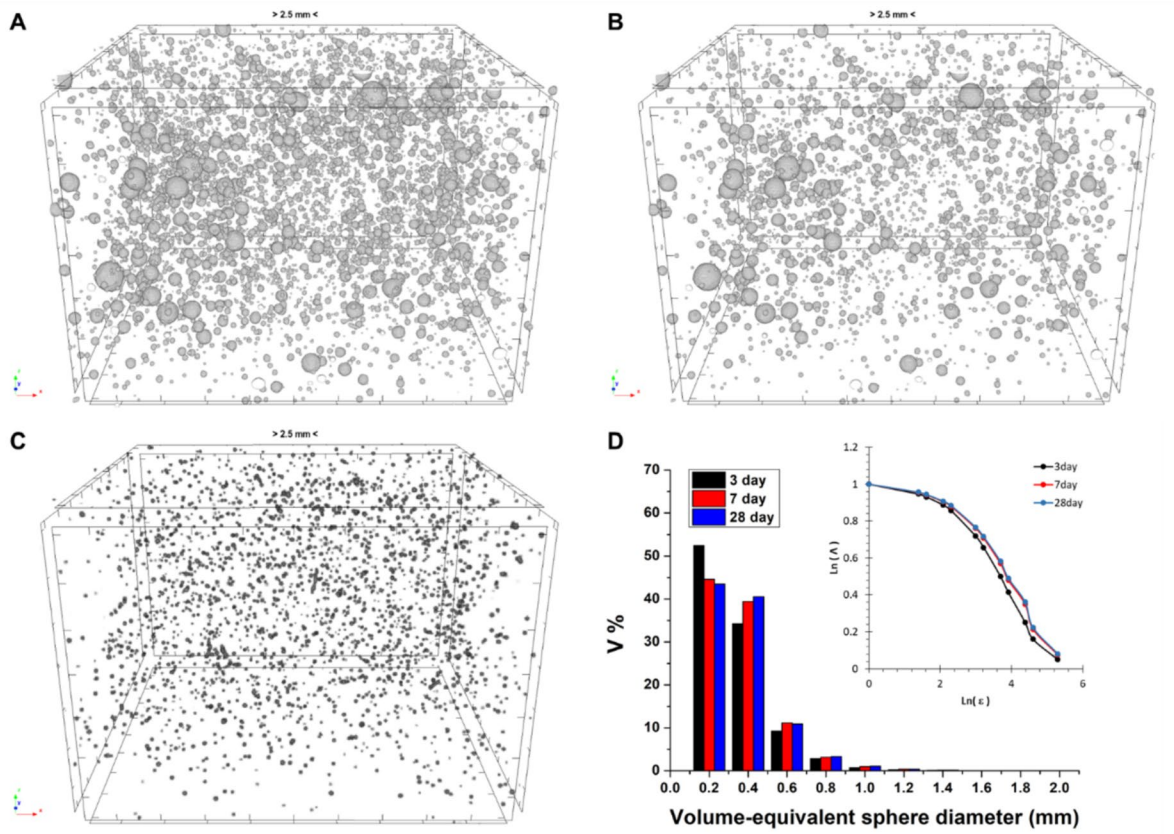

Fig. 4 Two-dimensional representation of 3D reconstructed closed pores in specimens after **A** 3 and **B** 28 days curing times, and **C** the pores that disappear during the curing between 3 and 28 days; effect of curing time **D** on pore size distribution and (insert) the lacunarity of closed pores

Table 3 Porosity analysis of the samples at different cure times

	3 days	7 days	28 days
Total porosity (%)	1.22	0.76	0.7
Number of closed pores	7743	4210	3822
Volume of closed pores (mm^3)	186.0	120.3	111.9
Vanished pores (mm^3)	–	6.6	7.3

was only 7.3 mm^3. Figure 5 shows the same pores (Fig. 5A, B) and their size distribution (Fig. 5C) after 3 and 28 days. The 3D volume-rendered images show that the size of the pores decreases during the curing process. Figure 5B shows the largest pore, whose volume has decreased by almost 17%, while the total pore volume has decreased by around 38% during curing. The scale of the reduction is consistent with the volume equivalent sphere diameter distribution.

3.3 Porosity analysis of the broken samples

The porosity of concrete also affects its physical properties, such as density, fracture toughness, thermal conductivity, etc. The study of the fracture mechanism of concrete has been a long-standing field of research, but computed tomography has added new, useful details to this field. Uniaxial compression tests were performed to uncover possible differences between the porosity of the broken sections and the residual hourglass-shaped piece (Fig. 6). The investigation of the final, hourglass-shaped specimens provided an opportunity to compare the pore structure of the remaining pieces and the broken fragments. As the samples were in fragments after the compression

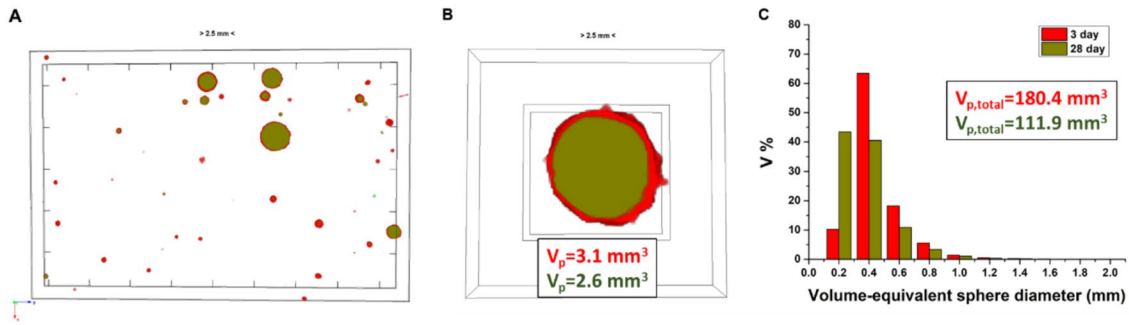

Fig. 5 **A**–**B** an example of the 3D rendered image of the pore after 3 and 28 days of curing, and **B** the size change of the remaining pores during curing. The red color indicates a 3-day sample, and the green color indicates a 28-day sample

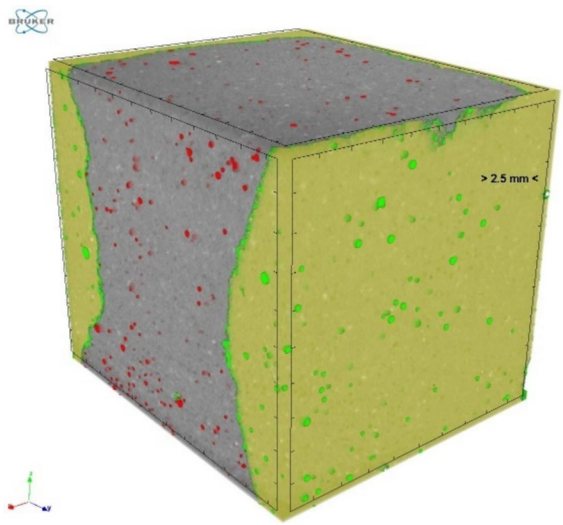

Fig. 6 Representative volume-rendered micro-CT image showing the hourglass-shaped breaking pattern of the concrete cubes

tests, Parafilm wrapping was employed to hold the pieces together, which facilitated the micro-CT measurements of the whole cube and visualization of the cracks.

Notable differences were found between the inner and outer parts of the cubes, as outlined in Table 4. The parts that broke off displayed a higher porosity volume compared to the remaining hourglass-shaped parts, with an increase of approximately 18%. Additionally, the average pore volume was higher, measuring at 0.08 mm^3, compared to the original value of 0.06 mm^3. However, the number of volumetric pore density (number of pores/mm^3) did not show a significant difference. It should be emphasized that the exact number of pores holds a smaller significance in this instance since the remaining and broken parts differ in volume.

The analysis of individual objects reveals that pores with the largest diameter tend to be present in the parts that break off, as illustrated in Fig. 7. In contrast, the hourglass-shaped parts tend to exhibit smaller pore sizes than the whole samples or the broken parts. In detail, during compression tests, 13.7%

Table 4 Porosity analysis of the TC, and comparison of the broken parts, the remaining hourglass-shaped parts, and the intact original total sample volume

	Total	Hourglass-shaped residual	Part that broke off
Total porosity (%)	1.46 ± 0.11	1.35 ± 0.17	1.65 ± 0.08
Number of closed pores	4191 ± 232	2510 ± 74	1548 ± 165
Volume of closed pores (mm^3)	294.2 ± 21.8	154.2 ± 20.5	139.9 ± 9.4
Number of pores/mm^3	0.19 ± 0.01	0.18 ± 0.01	0.18 ± 0.02
Average pore volume (mm^3)	0.070 ± 0.004	0.061 ± 0.006	0.084 ± 0.009
Average pore diameter (mm)	0.51 ± 0.03	0.49 ± 0.05	0.54 ± 0.06

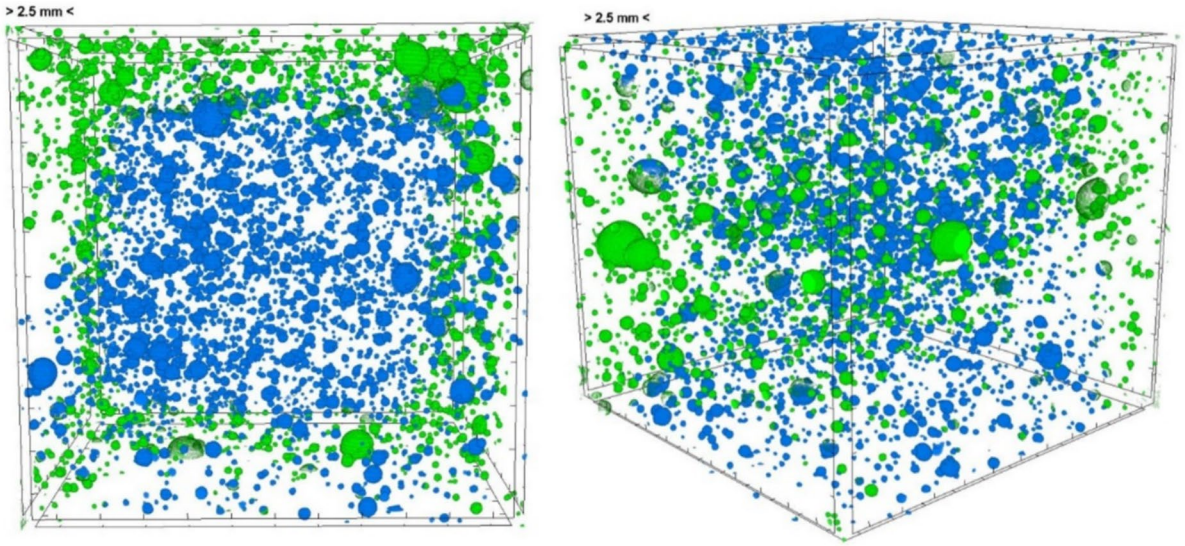

Fig. 7 The pore structure of a representative TC sample from top (left) and side view (right): green represents the pores of the broken parts, while blue represents the pores of the remaining hourglass-shaped part

of large pores (> 1 mm in diameter) break in the samples, while only 3.2% of all pores break (Fig. 8). Interestingly, the largest pore either breaks during compression or becomes a part of the broken part in 80% of the cases.

This study clearly shows that the remaining and the broken part have a different pore structure, suggesting that the pore structure of the concrete has an influence on the fracture mechanism. This is in agreement with observations in the literature. Huang et al. have

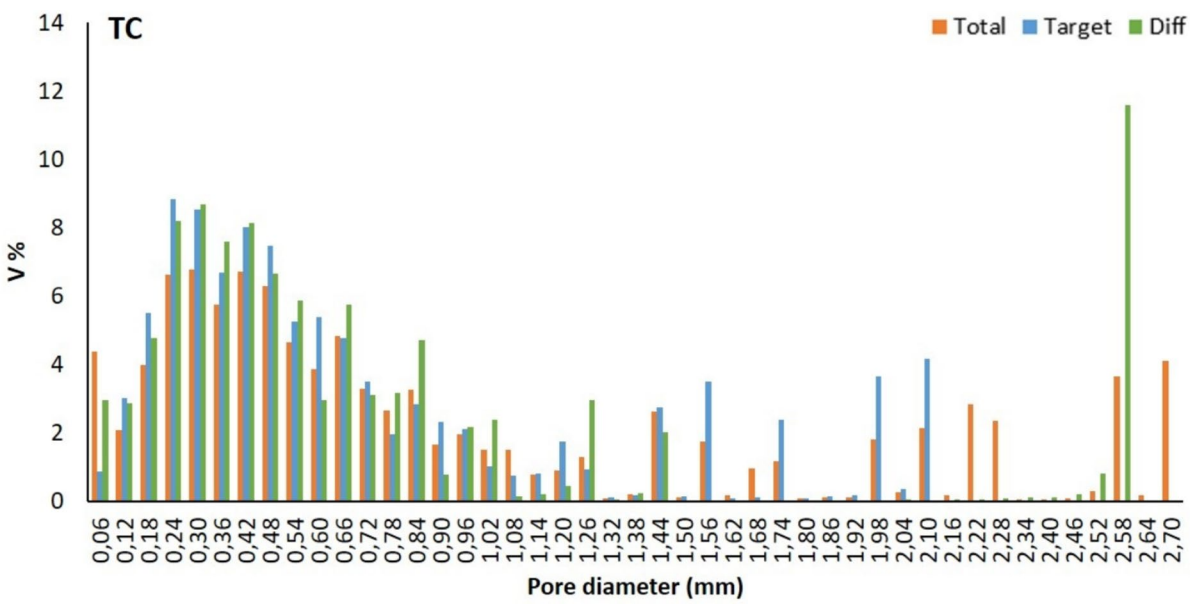

Fig. 8 Pore size distribution of **A** TC and **B** SPC for the whole sample (total), the broken parts (diff), and the remaining hourglass-shaped parts (target)

demonstrated that the distribution of pores has a significant influence on the crack patterns and strength of concrete specimens [65]. Furthermore, Vu et al. emphasized the importance of quantifying the porosity and size distribution of pores in understanding the compressive strength of concrete [66]. Additionally, Yang et al. utilized X-ray microscopy to obtain the fracture and pore distribution characteristics of coal samples under the influence of axial stress, providing insights into the relationship between pore distribution and fracture behavior [67].

Recent X-ray micro-computed tomography studies have demonstrated the capability of resolving pore size distributions, porosity, and crack-related features in concrete and cementitious materials under varying mix designs and curing conditions [68–71]. These investigations clearly show that pore characteristics are sensitive to processing history, and the reduction in porosity and refinement of pore size observed in the present study are consistent with these recent findings. Nevertheless, most recent works focus primarily on static pore characteristics, such as porosity or pore size distribution, and do not explicitly examine how microstructural evolution processes, like curing and fracture, affect the spatial heterogeneity of the pore system in a scale-dependent manner. As a result, changes in heterogeneity are often inferred indirectly or remain qualitatively described.

In contrast, the present study follows the evolution of pore-system heterogeneity during curing and links it to fracture behavior by applying three-dimensional lacunarity analysis. This approach provides a quantitative and scale-sensitive description of heterogeneity and complements conventional pore metrics, enabling a process-oriented interpretation of concrete pore structure that extends beyond existing micro-CT studies.

4 Conclusions

The present study demonstrated that micro-CT measurements are an effective tool for analyzing the pore structure and distribution in concrete made from Portland composite cement and fine sand, both with and without the addition of superplasticizer. In addition to standard pore system metrics, the lacunarity function was shown to provide valuable insight into the heterogeneity of pore distribution. The analysis revealed that large pores exhibit greater heterogeneity compared to smaller ones. In superplasticized concrete, total lacunarity is predominantly influenced by small pores, whereas in conventional concrete, both large and small pores contribute equally.

Furthermore, the investigation into the curing process confirmed that concrete porosity decreases significantly within the first week, before stabilizing at a constant value, primarily due to pore shrinkage. Finally, it was demonstrated that CT measurements can be utilized not only to map the pore system in intact concrete cubes, but also to analyze fracture fragments from mechanical testing, offering valuable insights into the fracture mechanisms of concrete. These findings contribute to a more comprehensive understanding of pore evolution and distribution in concrete, which is crucial for improving its durability and mechanical performance.

Acknowledgements Project no. 2022-2.1.1-NL-2022-00012 has been implemented with support from the Ministry of Culture and Innovation of Hungary, funded under the 2022-2.1.1-NL funding scheme, financed by the National Research, Development and Innovation Fund.

Funding Open access funding provided by University of Szeged.

Data and code availability The data that support the findings of this study are available from the corresponding author upon reasonable request.

References

1. Ji Z, Li M, Su L, Pei Y (2020) Porosity, mechanical strength and structure of waste-based geopolymer foams by different stabilizing agents. Constr Build Mater

258:119555. https://doi.org/10.1016/j.conbuildmat.2020.119555
2. Higaeg M, Balac I, Grbovic A, Milovancevic M, Jelic M (2019) Numerical modeling of the porosity influence on strength of structural materials. Sci Sinter 51:459–467. https://doi.org/10.2298/SOS1904459H
3. Hao J-H, Chen Q, Hu K (2016) Porosity distribution optimization of insulation materials by the variational method. Int J Heat Mass Transf 92:1–7. https://doi.org/10.1016/j.ijheatmasstransfer.2015.08.076
4. Kearsley EP, Wainwright PJ (2001) Porosity and permeability of foamed concrete. Cem Concr Res 31:805–812. https://doi.org/10.1016/S0008-8846(01)00490-2
5. Netinger Grubeša I, Marković B, Vračević M, Tunkiewicz M, Szenti I, Kukovecz Á (2019) Pore structure as a response to the freeze/thaw resistance of mortars. Materials 12:3196. https://doi.org/10.3390/ma12193196
6. NetingerGrubeša I, Vračević M, Ducman V, Marković B, Szenti I, Kukovecz Á (2020) Influence of the size and type of pores on brick resistance to freeze-thaw cycles. Materials (Basel) 13:3717. https://doi.org/10.3390/ma13173717
7. Coletti C, Cultrone G, Maritan L, Mazzoli C (2016) Combined multi-analytical approach for study of pore system in bricks: how much porosity is there? Mater Charact 121:82–92. https://doi.org/10.1016/j.matchar.2016.09.024
8. Sola A, Nouri A (2019) Microstructural porosity in additive manufacturing: the formation and detection of pores in metal parts fabricated by powder bed fusion. J Adv Manuf Process. https://doi.org/10.1002/amp2.10021
9. Li D, Li Z, Lv C, Zhang G, Yin Y (2018) A predictive model of the effective tensile and compressive strengths of concrete considering porosity and pore size. Constr Build Mater 170:520–526. https://doi.org/10.1016/j.conbuildmat.2018.03.028
10. Namsone E, Šahmenko G, Korjakins A (2017) Durability properties of high performance foamed concrete. Procedia Eng 172:760–767. https://doi.org/10.1016/j.proeng.2017.02.120
11. Kumar R, Bhattacharjee B (2003) Study on some factors affecting the results in the use of MIP method in concrete research. Cem Concr Res 33:417–424. https://doi.org/10.1016/S0008-8846(02)00974-2
12. Donato ID, Lazzara G (2012) Porosity determination with helium pycnometry as a method to characterize waterlogged woods and the efficacy of the conservation treatments. Archaeometry 54:906–915. https://doi.org/10.1111/j.1475-4754.2011.00657.x
13. Arregui-Mena JD, Edmondson PD, Campbell AA, Katoh Y (2018) Site specific, high-resolution characterisation of porosity in graphite using FIB-SEM tomography. J Nucl Mater 511:164–173. https://doi.org/10.1016/j.jnucmat.2018.08.047
14. Shah SM, Crawshaw JP, Boek ES (2017) Three-dimensional imaging of porous media using confocal laser scanning microscopy. J Microsc 265:261–271. https://doi.org/10.1111/jmi.12496
15. Sasov A (2004) X-ray nanotomography. In: Dev. X-Ray Tomogr. IV, pp 201–211. https://doi.org/10.1117/12.559009
16. Vásárhelyi L, Kónya Z, Kukovecz Á, Vajtai R (2020) Microcomputed tomography–based characterization of advanced materials: a review. Mater Today Adv 8:100084. https://doi.org/10.1016/j.mtadv.2020.100084
17. Withers PJ, Bouman C, Carmignato S, Cnudde V, Grimaldi D, Hagen CK, Maire E, Manley M, Du Plessis A, Stock SR (2021) X-ray computed tomography. Nat Rev Methods Prim 1:18. https://doi.org/10.1038/s43586-021-00015-4
18. du Plessis A, Olawuyi BJ, Boshoff WP, le Roux SG (2016) Simple and fast porosity analysis of concrete using X-ray computed tomography. Mater Struct Constr 49:553–562. https://doi.org/10.1617/s11527-014-0519-9
19. Bertoldi S, Farè S, Tanzi MC (2011) Assessment of scaffold porosity: the new route of micro-CT 9:165–175. https://doi.org/10.5301/JABB.2011.8863
20. Saxena N, Hofmann R, Alpak FO, Dietderich J, Hunter S, Day-Stirrat RJ (2017) Effect of image segmentation & voxel size on micro-CT computed effective transport & elastic properties. Mar Pet Geol 86:972–990. https://doi.org/10.1016/j.marpetgeo.2017.07.004
21. Da Wang Y, Shabaninejad M, Armstrong RT, Mostaghimi P (2021) Deep neural networks for improving physical accuracy of 2D and 3D multi-mineral segmentation of rock micro-CT images. Appl Soft Comput 104:107185. https://doi.org/10.1016/j.asoc.2021.107185
22. Perciano T, Ushizima D, Krishnan H, Parkinson D, Larson N, Pelt DM, Bethel W, Zok F, Sethian J (2017) Insight into 3D micro-CT data: exploring segmentation algorithms through performance metrics. J Synchrotron Radiat 24:1065–1077. https://doi.org/10.1107/S1600577517010955
23. Deboodt T, Wildenschild D, Ideker JH, Burkan Isgor O (2021) Comparison of thresholding techniques for quantifying portland cement hydrates using synchrotron microtomography. Constr Build Mater 266:121109. https://doi.org/10.1016/j.conbuildmat.2020.121109
24. Korfiatis VC, Tassani S, Matsopoulos GK (2017) An Independent Active Contours Segmentation framework for bone micro-CT images. Comput Biol Med 87:358–370. https://doi.org/10.1016/j.compbiomed.2017.06.016
25. Requist MR, Sripanich Y, Peterson AC, Rolvien T, Barg A, Lenz AL (2021) Semi-automatic micro-CT segmentation of the midfoot using calibrated thresholds. Int J Comput Assist Radiol Surg 16:387–396. https://doi.org/10.1007/s11548-021-02318-z
26. Rezaei F, Izadi H, Memarian H, Baniassadi M (2019) The effectiveness of different thresholding techniques in segmenting micro CT images of porous carbonates to estimate porosity. J Pet Sci Eng 177:518–527. https://doi.org/10.1016/j.petrol.2018.12.063
27. Otsu N (1979) A threshold selection method from gray-level histograms. IEEE Trans Syst Man Cybern 9:62–66. https://doi.org/10.1109/TSMC.1979.4310076
28. Borrelli P, Kaboteh R, Enqvist O, Ulén J, Trägårdh E, Kjölhede H, Edenbrandt L (2021) Artificial intelligence-aided CT segmentation for body composition analysis: a validation study. Eur Radiol Exp. https://doi.org/10.1186/s41747-021-00210-8
29. Kopp R, Joseph J, Ni X, Roy N, Wardle BL (2022) Deep learning unlocks X-ray microtomography segmentation of multiclass microdamage in heterogeneous materials. Adv Mater. https://doi.org/10.1002/adma.202107817

30. Dorey RA, Yeomans JA, Smith PA (2002) Effect of pore clustering on the mechanical properties of ceramics. J Eur Ceram Soc 22:403–409. https://doi.org/10.1016/S0955-2219(01)00303-X
31. Mandelbrot BB (1982) The fractal geometry of nature. Freeman, San Francisco
32. Gefen Y, Meir Y, Mandelbrot BB, Aharony A (1983) Geometric implementation of hypercubic lattices with noninteger dimensionality by use of low lacunarity fractal lattices. Phys Rev Lett 50:145–148. https://doi.org/10.1103/PhysRevLett.50.145
33. Majumder SR, Bandyopadhyay T, Ghosh SK (2005) Mechanical stability of end-linked polymer gel. Radiat Phys Chem 74:252–260. https://doi.org/10.1016/j.radphyschem.2005.04.018
34. Majumder SR, Mazumdar S (2007) Mechanical breakdown of trabecular bone: dependence on microstructure. Physica A Stat Mech Appl 377:559–564. https://doi.org/10.1016/j.physa.2006.11.069
35. Allain C, Cloitre M (1991) Characterizing the lacunarity of random and deterministic fractal sets. Phys Rev A 44:3552–3558. https://doi.org/10.1103/PhysRevA.44.3552
36. Hanen A, Imen B, Asma BA, Patrick D, Hédi BM (2009) Multifractal modelling and 3D lacunarity analysis. Phys Lett A 373:3604–3609. https://doi.org/10.1016/j.physleta.2009.07.087
37. Sebők D, Vásárhelyi L, Szenti I, Vajtai R, Kónya Z, Kukovecz Á (2021) Fast and accurate lacunarity calculation for large 3D micro-CT datasets. Acta Mater 214:116970. https://doi.org/10.1016/j.actamat.2021.116970
38. Roy A, Perfect E, Dunne WM, McKay LD (2014) A technique for revealing scale-dependent patterns in fracture spacing data. J Geophys Res Solid Earth 119:5979–5986. https://doi.org/10.1002/2013JB010647
39. Plotnick RE, Gardner RH, Hargrove WW, Prestegaard K, Perlmutter M (1996) Lacunarity analysis: a general technique for the analysis of spatial patterns. Phys Rev E 53:5461–5468. https://doi.org/10.1103/PhysRevE.53.5461
40. Dos Santos CR, Antonino ACD, Heck RJ, de Lucena LRR, de Oliveira ACH, da Silva ASA, Stosic B, Menezes RSC (2020) 3D soil void space lacunarity as an index of degradation after land use change. Acta Sci Agron 42:1–9. https://doi.org/10.4025/actasciagron.v42i1.42941
41. Xia Y, Cai J, Perfect E, Wei W, Zhang Q, Meng Q (2019) Fractal dimension, lacunarity and succolarity analyses on CT images of reservoir rocks for permeability prediction. J Hydrol 579:124198. https://doi.org/10.1016/j.jhydrol.2019.124198
42. Liu K, Ostadhassan M (2017) Quantification of the microstructures of Bakken shale reservoirs using multi-fractal and lacunarity analysis. J Nat Gas Sci Eng 39:62–71. https://doi.org/10.1016/j.jngse.2017.01.035
43. N'Diaye M, Degeratu C, Bouler JM, Chappard D (2013) Biomaterial porosity determined by fractal dimensions, succolarity and lacunarity on microcomputed tomographic images. Mater Sci Eng C Mater Biol 33:2025–2030. https://doi.org/10.1016/j.msec.2013.01.020
44. Massai D, Pennella F, Gentile P, Gallo D, Ciardelli G, Bignardi C, Audenino A, Morbiducci U (2014) Image-based three-dimensional analysis to characterize the texture of porous scaffolds. Biomed Res Int 2014:1–8. https://doi.org/10.1155/2014/161437
45. Chung SY, Kim JS, Stephan D, Han TS (2019) Overview of the use of micro-computed tomography (micro-CT) to investigate the relation between the material characteristics and properties of cement-based materials. Constr Build Mater 229:1–13. https://doi.org/10.1016/j.conbuildmat.2019.116843
46. da Silva ÍB (2018) X-ray computed microtomography technique applied for cementitious materials: a review. Micron 107:1–8. https://doi.org/10.1016/j.micron.2018.01.006
47. Brisard S, Serdar M, Monteiro PJM (2020) Multiscale X-ray tomography of cementitious materials : a review. Cem Concr Res 128:105824. https://doi.org/10.1016/j.cemconres.2019.105824
48. du Plessis A, Boshoff WP (2019) A review of X-ray computed tomography of concrete and asphalt construction materials. Constr Build Mater 199:637–651. https://doi.org/10.1016/j.conbuildmat.2018.12.049
49. Lian C, Zhuge Y, Beecham S (2011) The relationship between porosity and strength for porous concrete. Constr Build Mater 25:4294–4298. https://doi.org/10.1016/j.conbuildmat.2011.05.005
50. Chung S-Y, Kim J-S, Han T-S (2019) Effects of void clustering on the thermal and mechanical properties of concrete evaluated using numerical methods. Multiscale Sci Eng 1:196–209. https://doi.org/10.1007/s42493-019-00017-1
51. Zhang M (2017) Pore-scale modelling of relative permeability of cementitious materials using X-ray computed microtomography images. Cem Concr Res 95:18–29. https://doi.org/10.1016/j.cemconres.2017.02.005
52. Chung S-Y, Lehmann C, Abd Elrahman M, Stephan D (2017) Pore characteristics and their effects on the material properties of foamed concrete evaluated using micro-CT images and numerical approaches. Appl Sci 7:550. https://doi.org/10.3390/app7060550
53. Jain A, Gencturk B (2021) Multiphysics and multiscale modeling of coupled transport of chloride ions in concrete. Materials (Basel) 14:1–29. https://doi.org/10.3390/ma14040885
54. Castillo D, Nguyen THA, Niiranen J (2021) Spatially random modulus and tensile strength: contribution to variability of strain, damage, and fracture in concrete. Int J Damage Mech 30:1497–1523. https://doi.org/10.1177/10567895211013081
55. Le TD, Lehner P, Konečnỳ P (2019) Probabilistic modeling of chloride penetration with respect to concrete heterogeneity and epoxy-coating on the reinforcement. Materials (Basel). https://doi.org/10.3390/ma1224068
56. Gao W, Zhang C, Song G, Li H-N (2021) Time reversal damage localization in concrete based on two-dimensional meso-scale modeling. Struct Health Monit 20:188–201. https://doi.org/10.1177/1475921720918374
57. Carpinteri A, Cornetti P, Puzzi S (2006) Scaling laws and multiscale approach in the mechanics of heterogeneous and disordered materials. Appl Mech Rev 59:283–305. https://doi.org/10.1115/1.2204076

58. Chongkai L, Weiping Z, Xianglin G, Qinghua H (2018) Probability Distribution of Cross-sectional radius of Corroded Steel Bars in Concrete and Its application. MATEC Web Conf 199:04008. https://doi.org/10.1051/matecconf/201819904008
59. Chhun P, Buffo-Lacarriere L, Sellier A (2016) Material and geometric heterogeneity consideration for cracking risk prediction of young age behavior of experimental massive reinforced concrete structure. Key Eng Mater 711:900–907. https://doi.org/10.4028/www.scientific.net/KEM.711.900
60. Gabriel-Wettey FKN, Appiadu-boakye K, Anewuoh F (2021) Impact of curing methods on the porosity and compressive strength of concrete. J Eng Res Rep 20:18–30. https://doi.org/10.9734/JERR/2021/v20i917371
61. Huang H, Qian C, Zhao F, Qu J, Guo J, Danzinger M (2016) Improvement on microstructure of concrete by polycarboxylate superplasticizer (PCE) and its influence on durability of concrete. Constr Build Mater 110:293–299. https://doi.org/10.1016/j.conbuildmat.2016.02.041
62. Khudhair MHR, Elyoubi MS, Elharfi A (2018) Study of the influence of water reducing and setting retarder admixtures of polycarboxylate"superplasticizers" on physical and mechanical properties of mortar and concrete. J Mater Environ Sci 9:56–65. https://doi.org/10.26872/jmes.2018.9.1.7
63. Feldkamp LA, Davis LC, Kress JW (1984) Practical cone-beam algorithm. J Opt Soc Am A Opt Image Sci Vis 1:612–619. https://doi.org/10.1364/JOSAA.1.000612
64. Zhang Y, Kong X (2014) Influences of superplasticizer, polymer latexes and asphalt emulsions on the pore structure and impermeability of hardened cementitious materials. Constr Build Mater 53:392–402. https://doi.org/10.1016/j.conbuildmat.2013.11.104
65. Huang Y, Yang Z, Ren W, Liu G, Zhang C (2015) 3D meso-scale fracture modelling and validation of concrete based on in-situ X-ray Computed Tomography images using damage plasticity model. Int J Solids Struct 67:340–352. https://doi.org/10.1016/j.ijsolstr.2015.05.002
66. Vu C-C, Plé O, Weiss J, Amitrano D (2020) Revisiting the concept of characteristic compressive strength of concrete. Constr Build Mater 263:120126. https://doi.org/10.1016/j.conbuildmat.2020.120126
67. Yang Q, Yu Y, Cheng W, Cui W, Xin Q, Gao C, Zheng L (2022) Porosity and fracture changes of coal under uniaxial strain conditions based on the X-ray microscopic imaging technology. Energy Fuels 36:320–332. https://doi.org/10.1021/acs.energyfuels.1c03463
68. Xiao S, Yang J, Liu Z, Yang W, He J (2024) Effects of curing conditions on pore structure of ultra-high-strength shotcrete (UHSSC) based on X-ray computed tomography. Materials 17:4094. https://doi.org/10.3390/ma17164094
69. Kovács A (2024) Study of the gap parameters of cement mortar specimens based on X-ray tomography. Period Polytech Chem Eng 68:523–530. https://doi.org/10.3311/PPch.38379
70. Mishra A, Carrara P (2026) Fracture in concrete: X-ray tomography with in-situ testing, digital volume correlation and phase-field modeling. Cem Concr Res 199:108012. https://doi.org/10.1016/j.cemconres.2025.108012
71. Jiang Z, Pan Y, Fu C, Li W, Wang Y, Long W (2023) Three-dimensional pore structure characterization of cement paste by X-ray computed tomography (XCT) and focused ion beam / scanning electron microscopy (FIB / SEM). Constr Build Mater 383:131379. https://doi.org/10.1016/j.conbuildmat.2023.131379